Syngas Evolution from CO2 Electroreduction by Porous Au Nanostructures

Luca Mascaretti, Alessandro Niorettini, Beatrice Roberta Bricchi, Matteo Ghidelli, Alberto Naldoni, Stefano Caramori, Andrea Li Bassi, Serena Berardi

Syngas evolution from CO_2 electroreduction by porous Au nanostructures

Luca Mascaretti,[a,b] Alessandro Niorettini,[c] Beatrice Roberta Bricchi,[a] Matteo Ghidelli,[a,d] Alberto Naldoni,[b] Stefano Caramori,[c] Andrea Li Bassi,[a,*] Serena Berardi[c,*]

[a] Micro- and Nanostructured Materials Laboratory, Department of Energy, Politecnico di Milano, Via Ponzio 34/3, 20133 Milano, Italy

[b] Regional Centre of Advanced Technologies and Materials, Faculty of Science, Palacký University, Šlechtitelů 27, 78371 Olomouc, Czech Republic

[c] Department of Chemical and Pharmaceutical Sciences, University of Ferrara, Via Luigi Borsari 46, 44121 Ferrara, Italy

[d] Department of Structure and Nano/-Micromechanics of Materials, Max-Planck-Institut für Eisenforschung GmbH, Max-Planck Straße 1, 40237 Düsseldorf, Germany

[*] Corresponding authors: andrea.libassi@polimi.it; serena.berardi@unife.it

Abstract

The electrocatalytic reduction of CO_2 recently emerged as a viable solution in view of changing the common belief and considering carbon dioxide as a valuable reactant instead of a waste product. In this view, we herein propose the one-step synthesis of gold nanostructures of different morphology grown on fluorine-doped tin oxide electrodes by means of pulsed laser deposition. The resulting cathodes are able to produce syngas mixtures of different compositions at overpotentials as low as 0.31 V in CO_2-presaturated aqueous media. Insights on the correlation between the structural features/morphology of the cathodes and their catalytic activity is also provided, confirming recent reports on the remarkable sensitivity towards CO production for gold electrodes exposing under-coordinated sites and facets.

Keywords

CO_2 reduction; pulsed laser deposition; nanoporous films; Au nanostructures; electrocatalysis

1. Introduction

The containment of the greenhouse effect and of serious alterations to ecosystems will likely require not only a net reversal of the currently increasing carbon dioxide (CO_2) emission trend, but also an extensive sequestration of this gas from the atmosphere.[1,2] In this context, the conversion of CO_2 in alternative fuels by electrochemical reduction represents an intriguing strategy towards the establishment of a virtuous circle,[3,4,5,6,7,8,9] especially if the use of an electrical grid powered by renewable sources is envisaged. Furthermore, provided the use of suitable metallic electrodes, this approach is known to yield different kinds of products,[3,10,11] some of which (such as carbon monoxide, formate, methane and methanol) would fit in the currently available infrastructures for the storage and transport of fossil fuels.

At the same time, CO_2 reduction is a challenging reaction involving several open issues that must be faced in view of a possible industrial implementation. First of all, it is a slow electrochemical process, involving multiple electron and proton transfers, as well as the adsorption of both the gaseous substrate and the reaction intermediates on electrodic metal surfaces.[3] Furthermore, since CO_2 electroreduction is most practically achieved in aqueous electrolytes, with reduced environmental impact with respect to organic solvents, the competition of proton reduction to H_2 is often substantial, jeopardizing the reaction selectivity.[12] The limitation of the proton reduction pathway is particularly challenging also in view of the slow dissolution rate of CO_2 in water and its scarce overall solubility (34 mM).[3] Nevertheless, the concomitant hydrogen evolution can be valorised in view of syngas production, i.e. a mixture of CO and H_2 instrumental in industrial processes, such as the Fischer-Tropsch synthesis. In particular, different CO/H_2 ratios allow for the production of different kinds of chemicals, ranging from liquid fuels (gasoline and diesel) to olefins, methanol, and methane, depending on the catalyst and the reaction conditions.[13,14,15]

From the mechanistic point of view, the first monoelectronic step of CO_2 electroreduction is thermodynamically very demanding (–1.9 V vs the Normal Hydrogen Electrode, NHE), since significant geometric rearrangements are involved in the transformation of the linear substrate in the bent radical anion, $CO_2^{\bullet-}$. Nevertheless, the coordination of the CO_2 molecule on electrodic surfaces can effectively mitigate this thermodynamic requirement. Indeed, several metals can effectively stabilize not only $CO_2^{\bullet-}$,[16] but also other key intermediates for the further (multielectronic) reduction reactions. Among them, *CO, *COOH and *CHO are formed via proton-electron transfer mechanisms[17] (the asterisk denotes a site on the electrodic surface). On the other hand, an optimal binding strength between the intermediates and the metal surface, i.e. not

hampering either the coordination or the product release, is crucial in terms of the overall catalytic activity, which is usually assessed through volcano plots (Sabatier principle).[17] As far as CO binding energy is concerned, the top of the volcano is occupied by gold,[4] which almost selectively forms carbon monoxide as the main CO_2 reduction product.[3] Smaller amounts of formic acid [3] and methanol [18,19] have been also detected respectively at low and high overpotentials.

Several reports evidenced the importance of nanostructuring the Au-based cathodic interfaces in order to boost CO formation over the competitive proton reduction in aqueous media. Highly-effective nanostructured Au cathodes typically exhibit: (i) metastable surface structures;[20] (ii) engineered high-index facets and features;[21,22] (iii) local changes in the electric double layer near the cathode surface,[23,24] and/or in the local pH of the electrolyte;[25] (iv) under-coordinated sites, including grain boundaries.[25,26,27,28] The latter has been recently identified as the most relevant feature for an efficient CO formation process by the Chorkendorff group. Through selective poisoning experiments, the authors could indeed prove that surface sites with high coordination numbers are ca. one order of magnitude less active for CO evolution than the under-coordinated sites, confirming the structure sensitivity of the CO_2 electroreduction process.[29] Higher selectivity and faster kinetics for CO production by low-coordinated Au(110) electrodes have been also confirmed by online electrochemical mass spectrometry.[30]

Engineered Au morphologies aimed at maximizing CO selectivity have been prepared through the most various synthetic strategies, including: (i) oxidation/re-reduction of Au foils,[20] also promoted by O_2 plasma treatments;[31] (ii) electroplating onto host templates;[32] (iii) optimized electrodeposition[24] or electrocrystallization with MHz potential oscillation;[33] (iv) electron beam deposition [25,26,34] and (v) deposition of preformed Au nanostructures on conductive electrodes.[22,35,36] In this context, a straightforward one-step synthesis of porous Au structures with easily tunable morphology (upon appropriately changing the process parameters) and not involving substrate limitations or thermal treatments, appears intriguing. These conditions could be fulfilled by Pulsed Laser Deposition (PLD), a highly versatile technique for the production of nanostructured films [37] or nanoparticles [38] of virtually any material, including metals,[39] alloys,[40] semiconductor oxides,[41] and carbon.[42] Highly porous structures are typically achieved by performing the laser ablation in the presence of a background gas and the resulting morphology can be easily tuned by controlling the gas pressure and/or the target-to-substrate distance.[41,43,44] Recently, some of us also showed that PLD can be used to produce Au nanoparticles with a precise control of size and

substrate coverage, while reporting their integration within nanostructured TiO_2 film by single step deposition.[39,41]

In this contribution, we report on the pulsed laser deposition of two different kinds of porous Au-nanostructured thin films on fluorine-doped tin oxide (FTO) electrodes, and their use as cathodes for CO_2 reduction in aqueous electrolytes. The accurate tuning of the deposition parameters allowed for the one-step synthesis of two nanoscale morphologies, one with a quite regular columnar arrangement, and the other displaying a foamy tridimensional structure. The two nanoporous catalysts enabled the formation of syngas ($CO+H_2$) mixtures of different composition, together with small amounts of formic acid, both outperforming a planar gold foil used as reference. Manifold set-ups and technological solutions for the electrochemical syngas preparation have been reported to date.[45,46,47,48,49] Among them, the electrochemical generation of syngas mixtures at low overpotentials suits well in a CO_2 valorization scenario, especially considering that one of the major costs in the whole Fischer-Tropsch processes is the syngas production itself (usually originating from methane or coal via steam reforming [50]).

2. Experimental Section

2.1. Materials. TEC 8 (8 Ω/sq) fluorine doped tin oxide (FTO) conductive glass slides were purchased from Pilkington. FTO slides were cleaned by 10 min sonication in an Alconox® aqueous solution, followed by 10 min sonication in 2-propanol. Gold foil (0.05 mm thick, 99.95%) and Nafion® N-117 membrane (0.180 mm thick) were purchased from Alfa Aesar. Gold foils were cleaned according to literature procedures.[20] Cr grains (99.99%) were purchased from Ista (Faenza), while CO_2 (> 99.9%) from SOL group. CO (99.0+%), NaOH (98%), 2-propanol, Alconox® and spectroscopic grade acetonitrile were purchased from Sigma Aldrich. $KHCO_3$ (99.5%) and KPF_6 (>98%) were respectively purchased from Riedel-De Haen and Fluka, while $Pb(NO_3)_2$ (99%) was purchased from Carlo Erba. Unless otherwise stated, all chemicals were used without additional purification. All electrolytic solutions were prepared using reagent grade water (Millipore, 18 MΩ·cm resistivity).

2.2. Cathode preparation and structural/morphological characterization. The cathodes consist in Au nanoporous films deposited on FTO substrates covered by a Cr adhesion layer, needed to avoid the detaching of the Au deposit during the electrochemical tests. The 5 nm-thick Cr layer was deposited on FTO substrates in an Edwards E306 thermal evaporator, by evaporating pure 99.99% Cr grains, while the equivalent thickness was controlled by means of a quartz microbalance. Au nanoporous films were then deposited on FTO substrates covered by the Cr interlayer via Pulsed

Laser Deposition (PLD). An Au (99.99%) target was ablated with a ns-pulsed laser (Nd:YAG, 2nd harmonic, λ=532 nm, repetition rate 10 Hz, pulse duration 5-7 ns); the laser fluence on the target was 2.3 J/cm^2, while the laser pulse energy was 150 mJ. The substrates were mounted on a rotating sample holder at fixed target-to-substrate distance of 5 cm. Depositions were performed at room temperature within a pure Ar background gas at two different pressures, 100 Pa and 1000 Pa, for a duration of 20 minutes (12000 shots). In order to distinguish Au nanoporous cathodes deposited at different Ar pressures, we name the films deposited at 100 and 1000 Pa as Col-Au and Foam-Au, respectively, as a result of their different morphology (vide infra). Both films were deposited also on Si(100) substrates added to the sample holder together with FTO substrates, for the purpose of film characterizations. These films were compared to the Au foil as a reference cathode with flat surface to evaluate the effect of the two different nanostructures obtained by PLD.

A field emission scanning electron microscope (FEG-SEM, Zeiss Supra 40) was used to perform morphological characterization on the films deposited on both Si and FTO substrates. In particular, the Si substrates were exploited for cross-sectional and top-view measurements, while the films deposited on FTO were scanned only in top-view. Moreover, the SEM micrographs were analyzed by ImageJ software to extract the substrate coverage and size of morphological features of different Au films.

Structural characterization of deposited Au films was carried out by X-ray diffraction (XRD). XRD patterns were collected using a high-resolution X-ray powder diffractometer (PANalytical X'Pert Pro MPD) using a Cu target (CuKα1 radiation –1.5406 Å) at room temperature. The measurements were performed in Bragg-Brentano (θ-θ) geometry with a step–scan technique in 2θ range of 25–85° with a step size of 0.016° and time/step of 40 s. The Bragg-Brentano geometry implies that X-ray diffraction occurs by the crystallographic planes that are parallel to the substrate, thus XRD peak intensities can provide information about the presence of preferential orientation of crystalline domains with respect to the substrate. The size of the Au crystalline domains was determined by using the Scherrer's equation on XRD fitted peaks.

Transmission electron microscopy (TEM) images were obtained with a TEM JEOL 2010 with LaB_6 emission gun operating at 160 kV. High-resolution images, energy dispersive X-ray spectroscopy (EDS) and STEM-HAADF (scanning transmission electron microscopy high-angle annular dark-field imaging) analysis were performed with a FEI Titan HRTEM microscope operating at 80 kV. The Au samples were scratched from the Si substrate and deposited on copper TEM grids.

X-ray photoelectron spectroscopy (XPS) measurements were performed with a PHI 5000 VersaProbe II XPS System (Physical Electronics) with monochromatic Al-kα source (15 kV, 50 W) and photon energy of 1486.7 eV. The spectra were evaluated with the MultiPak (Ulvak – PHI, Inc.) software.

2.3. Electrolyte purification. As widely reported, the presence of metal cation impurities (especially Fe^{2+}, Pb^{2+} and Zn^{2+}) in the electrolytic solutions used for the CO_2 electroreduction can result in unreliable results.[3] Indeed, under the cathodic conditions needed for the reaction to proceed, these metal cations can be reduced to the corresponding metals, and deposited onto the cathodic surface, leading to a significant modification of its catalytic properties. In particular, in the presence of these co-deposited metals, the overpotential for proton reduction is reduced, leading to an enhanced H_2 production over CO_2 reduction. Although nanostructured electrodes are less sensitive to this poisoning,[23] metal impurities were removed by pre-electrolyzing the electrolytic solution using two large-area titanium foils kept at –2 V under nitrogen bubbling for 15 h.[51] The effectiveness of the pre-electrolysis process has been proven by ICP-mass analysis, evidencing the absence of Fe^{2+}, Pb^{2+} and Zn^{2+} in the limits of the technique sensitivity (<0.5 ppm).

2.4. Electrochemical measurements.

- Determination of ECSA (ElectroChemical Surface Area) by double layer capacitance measurements. Experiments were carried out using an Autolab PGSTAT30 potentiostat in a 3-electrode set-up using a Pt-foil as the counter electrode, and a Saturated Calomel Electrode (SCE) bathed in a saturated KNO_3 solution as the reference. The electrolyte was prepared by dissolving 0.1 M KPF_6 in acetonitrile. The CV sampling mode was set to “normal linear scan”, thus allowing for a true analog linear sweep instead of the incremental potential steps of typical digitalized potentiostats (staircase mode). CV scans for Au foil, Col-Au and Foam-Au were recorded at scan rates in the range 5-50 mV/s, spanning ± 40 mV of the OCP, a range where no faradaic processes occur. The current values were divided by the geometric area of the electrodes, which was determined using a stereomicroscope (OPTIKA, at 10X magnification) with a millimeter sized transparent grid. From the CV traces, the capacitive current then was calculated as $(J_a - J_c)/2$, where J_a and J_c are, respectively, the anodic and cathodic current densities at OCP. The resulting values (in A/cm^2) were plotted against the scan rate of the CV experiments (in V/s) and the data fitted with a linear equation. The slope of the linear regression gives the capacitance of the electrode (in F/cm^2). Assuming the Au foil to be featureless (roughness factor, RF = 1 by definition), the RFs of Col-Au and Foam-Au electrodes can be

calculated by dividing the corresponding capacitance values by the capacitance of the Au foil used as the reference.

For each cathode, the OCP value was directly read on the potentiostat display after connecting all the three electrodes. The reading was stable. The OCP values for the different electrodes do not differ significantly in day to day use, with maximum variations within 70 mV. The ohmic resistance values, measured by electrochemical impedance spectroscopy, are in the range 14-16 Ω for Col-Au and Foam-Au samples, while 6-10 Ω were obtained for the Au foil.

- Determination of surface-exposed crystallographic facets: Pb underpotential deposition. Experiments were carried out in a 3-electrode set-up using a Pt-foil as the counter electrode, and a Saturated Calomel Electrode (SCE) as the reference. The electrolyte was prepared by dissolving 1 mM $Pb(NO_3)_2$ in 0.1 M NaOH, then purged with N_2 prior to CV scans.
- Determination of bridged CO (CO stripping). The surface coverage of CO molecules, kinetically inert and irreversibly bound to the nanoporous Au cathode (indicated in the main paper as CO_{bridge} species), can be estimated using the method described by the Surendranath group.[52] Briefly, the stripping cycles consisted in 3 successive linear scans: the 1st (up to 0.75 V vs SCE) allows for the registration of the oxidation peak due to the bielectronic stripping of the CO_{bridge} species; the 2nd starts at 0.75 V and stops at –0.14 V vs SCE, since scanning to more negative values would restore CO_{bridge} species;[52] the 3rd, from –0.14 V back to 0.75 V vs SCE, serves as the baseline for the integration of the 1st linear scan, in order to quantify the CO stripping charge, after correcting for the scan rate (0.05 V/s). The stripping cycles were recorded immediately after the bulk electroylses for the accumulation of the products.
- Products accumulation and analysis. Carbon dioxide electroreduction experiments were carried out in a modular custom made polymethylmetacrylate (PMMA) cell. An ionic transport membrane (Nafion® 117) divided the cell into two separated compartments. In the cathodic one, the working (Au-based cathodes) and the reference (SCE) electrodes were located, while in the anodic compartment the Pt counter electrode was immersed. Both the anolyte and the catholyte consisted in a pre-electrolyzed 0.5 M $KHCO_3$ aqueous solution, saturated with CO_2 (resulting pH = 7.4). The working electrodes were electrically connected to Cu wires using silver paint, then epoxy resin was used to isolate every part but the catalytic surface. We did not extend the scans to potentials lower than –0.62 V vs RHE since deterioration of the FTO substrates under exceedingly cathodic conditions can occur.

Stepped chronoamperometric experiments have been performed in order to accumulate the products. In particular, 270 s at the fixed cathodic bias needed for the reduction reaction are followed by 30 s at open circuit potential, in order to desorb the terminally bonded CO (CO_{term} in the main text) from the electrodic surfaces. For the sake of comparison with the majority of the literature, all the potential values applied in the CO_2 reduction experiments have been reported also versus the Reversible Hydrogen Electrode (RHE), using the formula:

$V\ (vs\ RHE) = V\ (vs\ SCE) + 0.24 + 0.059 \cdot pH$.

Unless otherwise stated, all the potential values concerning the CO_2 reduction experiments are given vs RHE in the text, while the figures report also a second potential axis, with values referred to the Saturated Calomel Electrode (SCE).

The cathodic compartment of the cell was connected to a headspace, from which the GC pump automatically collected samples for gas detection and quantification. The latter was performed by means of an Agilent Technologies 490 microGC equipped with a 5 Å molecular sieve column (10 m) and a thermal conductivity detector, using Ar as the carrier gas. 15 mL from the headspace were sampled by the internal GC pump and 9 μL were injected in the column, maintained at 90°C. The uninjected gas was then reintroduced in the cell in order to minimize its variation along the whole experiment.

Hydrogen was quantified using a response factor obtained through a galvanostatic electrolysis (10 mA, 1 hour) of a 0.1 M H_2SO_4 solution in the same electrochemical cell, using a Pt working electrode and assuming 100% faradaic efficiency of proton reduction. Carbon monoxide was quantified using a response factor obtained by injecting known amounts of CO in the electrochemical cell, then sampling the headspace. Quantification of formate was performed via ^{1}H-NMR spectroscopy (Agilent, 300 MHz). At the end of the pulsed-bias chronoamperometry experiments at the specific potential, the catholyte was sampled and known amounts of DMF and D_2O were added, respectively as the external standard and the locking solvent. The ^{1}H-NMR spectrum was acquired using a customized water suppression sequence, allowing for the minimization of the aqueous electrolyte signal. Formate was easily identified as the singlet peak at 8.3 ppm, and quantified by a comparative integration with the DMF peaks.

For all the products, the Faradic efficiency at the different applied biases could be calculated as follows:

$$FE = \frac{n \cdot F \cdot mol}{Qtot}\ \%$$

being mol the amount of product (determined as described above); n the number of electrons involved in the reduction reaction; F the Faraday constant; and Q_{tot} the total amount of charge passed at the interface during the pulsed bulk electrolyses experiments, obtained from the integration of the chronoamperometric curve over time.

3. Results and Discussion

3.1. Synthesis and characterization of the Au nanostructures. The nanostructured Au cathodes were deposited by means of pulsed laser deposition (PLD) on FTO substrates covered with a thin (5 nm) Cr adhesion layer prepared by thermal evaporation. Figure 1 shows the cross-sectional and top-view SEM images of Au films deposited at 100 and 1000 Pa of Ar, highlighting their different morphology as a function of the background deposition pressure. Indeed, the Au film deposited at 100 Pa shows a columnar structure for its whole thickness (Figures 1a and 1b); on the other hand, the Au film deposited at 1000 Pa exhibits a columnar-like structure only for a bottom ~80 nm-thick layer in contact with the substrate, while the main structure consists of a non-uniform foam-like morphology up to a few micrometers thick (Figures 1c and 1d). For these morphological features, in the following 100 Pa and 1000 Pa-deposited films are called Col-Au and Foam-Au, respectively. In particular, Col-Au film consists of ~200 nm thick and ~80 nm wide columns (Figure 1a), on average, separated by voids of the order of 10-15 nm (Figure 1b). On the other hand, the Foam-Au film shows a column-like bottom layer, sizing about 80 nm thick and 45 nm wide (Figure 1c), also separated by voids of the order of 10-15 nm (Figure 1d). Moreover, the foam-like structure on top is up to 3-4 μm thick and appears to be composed of sintered Au nanoparticles with size of a few tens of nm (average size 35 nm). Such foam-like domains cover ~20% of the substrate surface (Figure 1d).

The evident difference in morphology as a function of the background pressure is due to the coexistence of two different mechanisms of film growth during deposition, namely in-plume cluster nucleation and surface diffusion.[53,54] When other PLD parameters (e.g. laser energy and fluence, target-to-substrate distance) are kept constant, the predominance of one mechanism over the other is associated to the pressure level.[39] Indeed, during the PLD process, the laser-target interaction leads to target vaporization, which results in a plasma plume formation and consequent deposition of ablated species on the substrates.[38,43,55] The increment of background pressure from 100 to 1000 Pa has the effect of confining more effectively the plasma plume, as well as of slowing down the ablated species. Therefore, in-plume cluster nucleation phenomena are more predominant at 1000 Pa rather than at 100 Pa, resulting in the deposition of a more open and fluffier

Au nanoporous film with the different morphologies already described. The presence of the "compact" columnar bottom layer for the Foam-Au cathode deposited at 1000 Pa is probably related to the initial wetting of the substrate by means of the ablated Au.

Moreover, the background pressure level also affects the deposition rate, as the higher pressure means stronger scattering and thus a less directional ablation plume, which translates in higher dispersion within the deposition chamber and lower kinetic energy. The amount (mass density per unit surface) of Au deposited at the two pressure conditions estimated by means of a quartz microbalance was ~300 μg/cm^2 for Col-Au and ~150 μg/cm^2 for Foam-Au. The deposition of such tiny amounts of gold is indeed advantageous for the overall cost of the cathodes.

The structural characterization of Au samples was performed by means of X-ray diffraction (Figure 2). Specifically, both the Col-Au and Foam-Au films show peak positions in accordance with Au fcc structure; the higher signal-to-noise ratio of Col-Au indicates a better crystallinity for this film. The relative intensities of XRD peaks differ for both samples from those of reference Au powder with random orientation of crystalline domains. This is a clear indication of preferential crystalline domain growth with respect to the substrate. In detail, both films preferentially grow along the (111) direction; furthermore, for Col-Au, growth along the (220) direction also appears to be preferred with respect to the (200) one. On the other hand, the Au foil exhibits a preferential orientation along the (200) direction. The average size of Au crystalline domains was estimated by applying Scherrer's equation on Au (111) fitted peak, resulting in 37 nm and 29 nm for Col-Au and Foam-Au, respectively.

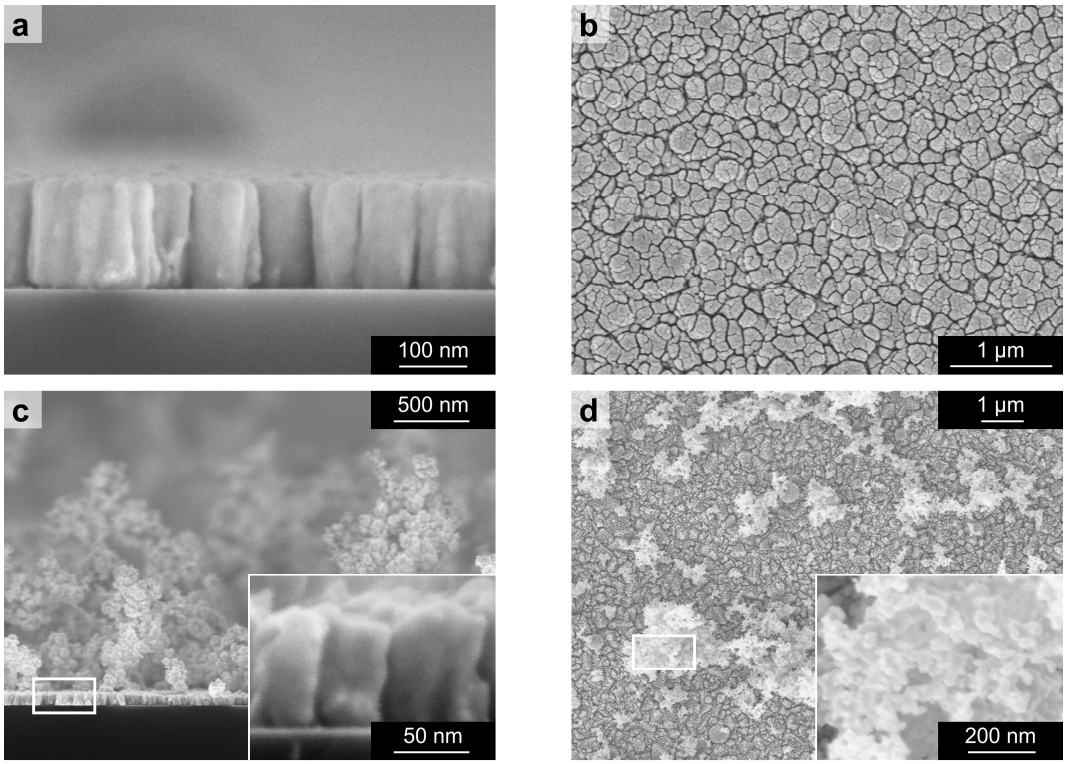

Figure 1. SEM images (top view and cross-section) of Au films: Col-Au deposited at 100 Pa (a, b) and Foam-Au deposited at 1000 Pa (c, d). Insets in (c, d) show images at higher magnification.

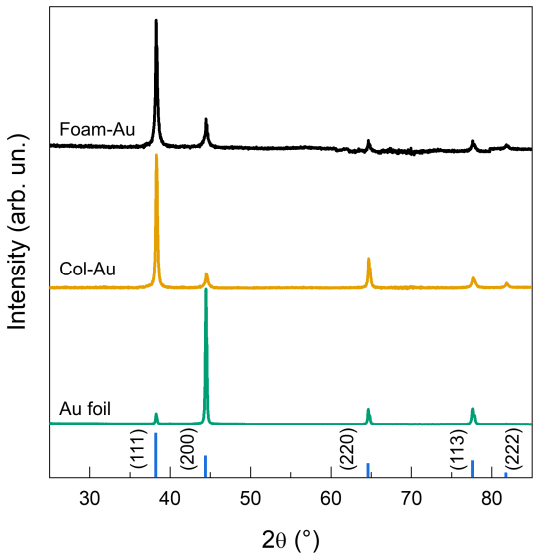

Figure 2. X-ray diffractograms of Col-Au, Foam-Au and Au foil; intensities have been normalized the (111) reflection (Col-Au and Foam-Au) and (200) reflection (Au foil). The characteristic peaks of the Au fcc structure in a powder system are reported as reference (PDF database card no. 00-004-0078); the height of the reference lines is proportional to the intensity of XRD reflections in reference Au powder.

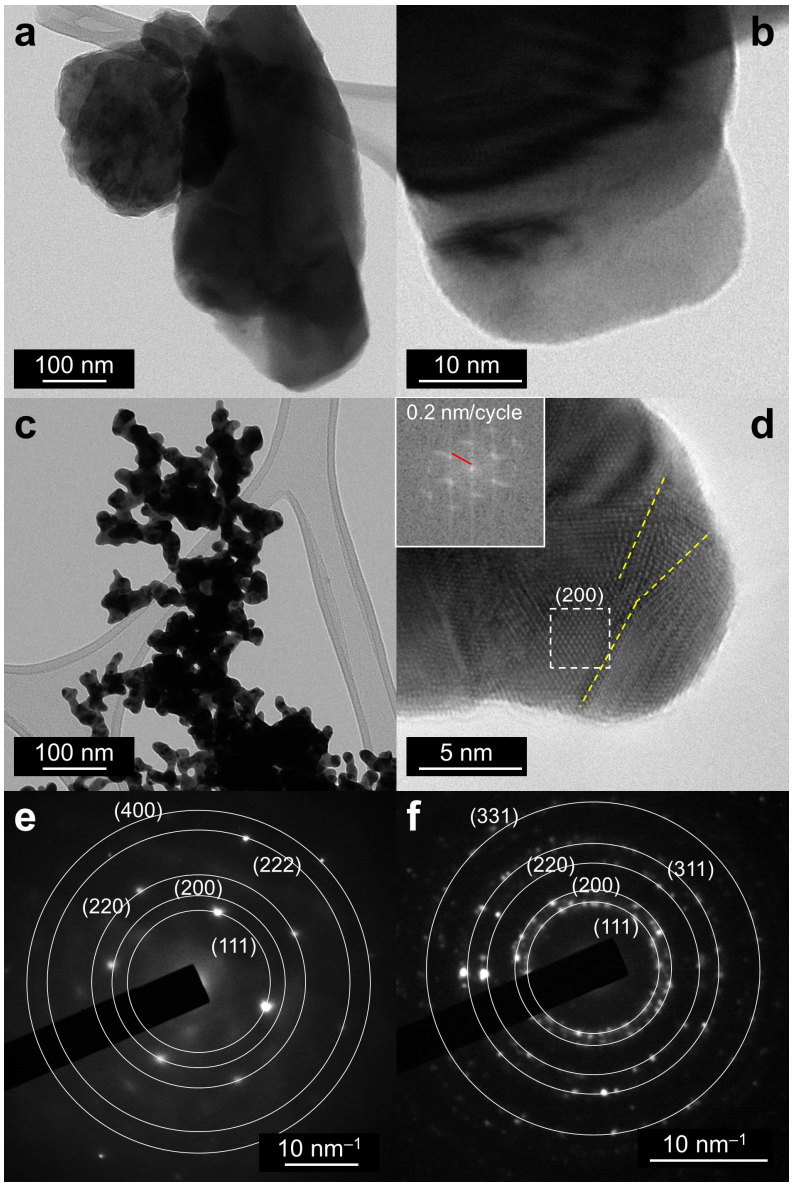

Figure 3. TEM images of Col-Au (a, b) and Foam-Au (c, d). The inset in (d) shows the Fourier transform of the atomically-resolved area highlighted by a dashed box; the yellow dashed lines mark grain boundaries. (e, f) Selected area electron diffraction (SAED) of the micrograph reported in Figures S1a and S1b respectively for Col-Au and Foam-Au, showing diffraction spots corresponding to the lattice planes of pure Au (camera length values of 2.25 and 1.30 were respectively used to correct the interplanar distance values).

TEM analysis was performed to gain more insights on the local structural properties of the nanostructured Au films (Figure 3). Figure 3a shows a portion of the Col-Au film, which appears dark due to its high density, thus preventing the acquisition of atomically-resolved images (Figure 3b). Figure 3c shows the foam-like structures growing on top of the Foam-Au film, while Figure 3d is a high-resolution TEM image with atomic resolution. In this case, grain boundaries could be discerned (yellow dashed lines in Figure 3d) as well as (200) planes at the surface. This observation suggests

the presence of randomly-oriented grains in the Foam-Au film. We anticipate that the presence of (200) facets can lead to relevant effects in terms of the Faradic efficiency towards CO_2 reduction to CO (see below).[29] Indeed, by analyzing larger areas with TEM to acquire SAED patterns (Figures S1a and 3e for Col-Au and Figures S1b and 3f for Foam-Au) a larger number of diffraction spots was found for the Foam-Au sample, thus confirming the above observation. Finally, the high level of purity of the Au nanostructured films was confirmed by Energy dispersive X-ray spectroscopy (EDS) mapping (see the STEM-high-angle angular dark-field (HAADF) micrograph in Figure S1c and the corresponding EDS map in Figure S1d).

The Col-Au and Foam-Au cathodes were initially characterized through different electrochemical techniques able to provide insights on both their active area and the exposed facets. As regards the first aspect, double layer capacitance (DLC) measurements are widely used,[56,57,58,59,60,61] since they represent a versatile non-destructive technique to estimate the electrochemical surface area (ECSA). However, it is worth noting that several processes involving ion transfer reactions at the interface (e.g. intercalation, specific adsorption, or surface proton transfer) can lead to additional contributions altering the actual capacitance values, especially in aqueous media. Thus, we performed the DLC experiments in acetonitrile, a polar aprotic solvent in which more uniform capacitance values for different materials can be obtained, following a recent procedure reported by the Surendranath group.[62] From the analysis of the cyclic voltammetries at different scan rates reported in Figure S2, compared to the ones obtained for a flat Au foil, we could estimate a roughness factor of 12.7 ± 3.1 for Col-Au and 9.1 ± 1.0 for Foam-Au (see also Table S1), most likely reflecting the trade-off between the opposite contributions due to the different morphology of the cathodes and their total gold loading. The values confirmed the high porosity of both the nanostructures, and resulted in line with roughness factors reported for cathodes with comparable morphologies.[34]

In order to gain insights into the distribution of the Au surface terminations of the two nanoporous structures, underpotential deposition (UPD) of Pb was performed. Results are reported in Figure 4, where the two reversible processes at $E_{1/2}$ = 0.35 V and 0.50 V vs RHE respectively correspond to Pb deposition and stripping from the (111) and (110) exposed facets of the Au cathodes, in agreement with XRD analyses (the (100) facet could be revealed at 0.40 V only for Au foil, reported as a reference).[26,32,63,64] For both Col-Au and Foam-Au, the relative amplitude of each wave was quite similar, suggesting a negligible dependence of the Au surface termination on the morphology of the cathodes. Similar behavior was previously observed in Au-inverse opal thin films,[32] as well as on

carbon nanotubes decorated with Au nanoparticles deposited via e-beam evaporation.[26] Anyway, in both Col-Au and Foam-Au morphologies the density of the (111) facets is higher with the respect to that of the (110). These results can translate in a reduced selectivity for the CO_2 versus the proton reduction reaction, since the more opened and under-coordinated (110) sites have been recently reported to be ca. 6 times more active for CO production than the (111) sites.[29]

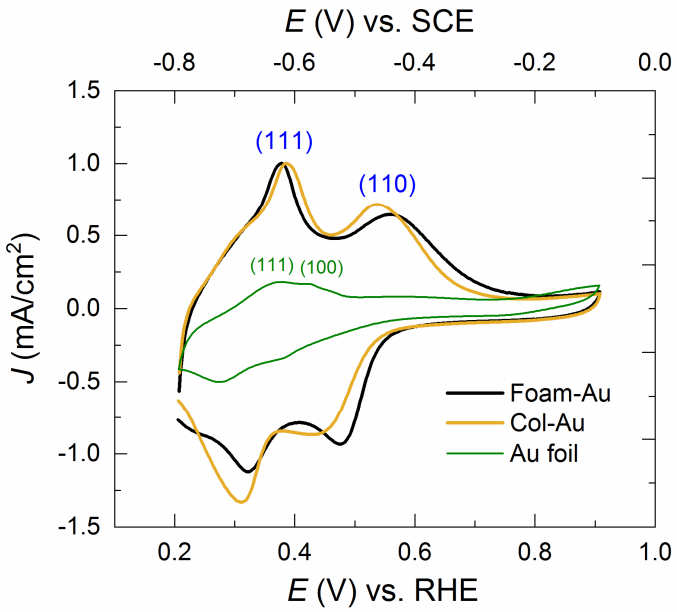

Figure 4. Pb UPD traces recorded in 1 mM $Pb(NO_3)_2$ + 0.1 M NaOH with 25 mV/s scan rate. (111) and (110) facet orientations are revealed at 0.35 and 0.50 V respectively, while (100) at 0.40 V. The curves for Foam-Au and Col-Au were normalized to match the peak heights of the (111) feature.

3.2. Electrochemical performances of the Au nanostructures. The so-prepared cathodes were tested as working electrodes in a custom-made electrochemical cell (see Experimental Section and Figure S3 for a more detailed description of the experimental set-up) using pre-electrolyzed 0.5 M $KHCO_3$ saturated with CO_2 as the electrolytic solution. The joined presence of these two species leads to the formation of a buffer system at pH 7.4, instrumental to avoid the build-up of a basic pH (and the consequent decrease of the dissolved CO_2) following the proton consumption during the electroreduction.

The cations of the electrolyte (K^+ in this specific case) are also known to participate in the buffering process, since their hydration shell can be polarized and then undergo hydrolysis under cathodic biases.[23,65,66] Furthermore, the K^+ absorbed on the electrodic surface may favor the stabilization of the intermediate anionic species via ion pairing [3,23,67] and, at the same time, decreasing the

competitive H_2 evolving reaction due to the build-up a more positive potential in the Helmholtz layer.[23,68]

Figure 5 shows the resulting J-E curves recorded at 10 mV/s while compensating for the ohmic drop. All the traces correspond to average values of at least 3 equivalent electrodes, and the corresponding standard deviations are also reported as error bars, evidencing the good reproducibility of the outcomes in terms of generated current. The performances of the two nanoporous cathodes were also compared those of a commercial Au foil as the standard reference, as well as to those of the bare Cr adhesion layer (J-E curves normalized for the ECSA are reported in Figure S4).

The analysis of the J-E curves revealed that the onset potential at which a significant cathodic current (in the specific, –0.5 mA/cm^2) starts to flow is –0.27 V for CoI-Au, corresponding to an overpotential $|\eta|$ = 0.16 V, being –0.11 V the thermodynamic potential for CO_2 reduction to CO. This onset value is pretty similar to the one registered for the pioneering oxide-derived Au nanostructures reported by the Kanan group.[20] Less negative onsets (–0.2 V) were however observed for very peculiar Au nanostructures, such as Au needles, for which high local electric fields arise, resulting in a higher local CO_2 concentration.[24]

On the other hand, the onset potential for Foam-Au was observed at –0.32 V ($|\eta|$= 0.21 V), with ca. –0.05 V cathodic onset shift with respect to CoI-Au. This shift can be due to subtle differences of the reaction kinetics at the two different interfaces, which can translate into different product distribution (vide infra). At the same time, the two nanoporous morphologies outperformed the Au foil, for which the current onset is observed at –0.42 V ($|\eta|$= 0.31 V), thus speaking in favour of improved kinetics in the nanostructured interfaces when compared to the flat Au surface. The Cr adhesion layer showed, as expected, a very retarded onset potential (at –0.61 V, $|\eta|$= 0.5 V) with the recorded current being essentially due to hydrogen generation.[3]

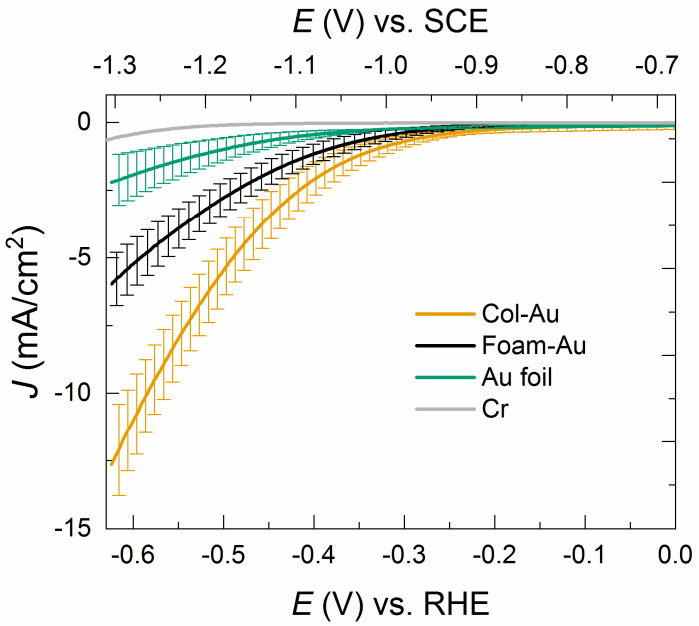

Figure 5. J-E characteristics for Col-Au (dark yellow), Foam-Au (black), Au foil (green) and Cr adhesion layer (gray) recorded in 0.5 M $KHCO_3$ saturated with CO_2 (pH 7.4), normalized for the geometric area and corrected for the iR-drop. The stable response (i.e. the 2nd of successive J-E cycles) of at least 3 electrodes has been averaged, and the corresponding curves are reported, together with the error bars.

The catalytic activity, in terms of generated current, follows the trend Au foil < Foam-Au < Col-Au, with the latter reaching up to –12.5 mA/cm^2 at –0.62 V. However, the ultimate assessment of the catalytic performances of the nanoporous cathodes must be done after the evaluation and quantification of the reduction products.

To this end, we performed chronoamperometric measurements under different potentials (Figure S5), since the distribution of CO_2 reduction products is known to change upon varying the applied bias. However, while performing these experiments, we noticed a progressive decrease in the cathodic currents, which we attributed to a partial poisoning of the cathodic surfaces. This behavior had been already reported for Au surfaces, and ascribed to different kind of adsorbed species, either potassium and/or carbon deposits,[69] or the produced CO itself.[52] In particular, terminally bonded CO species (CO_{term}) have been reported to be only reversibly absorbed on Au surface (lowering however the fraction of sites available for the catalysis), so they can be easily removed under open circuit potential (OCP) conditions. Indeed, when the chronoamperometric protocol was modified introducing short reconditioning steps at OCP, the initial current density values for both Foam-Au and Col-Au were restored (see Figure S5), allowing for the assessment of the medium term stability of the cathodes, as well as for the accumulation of sufficient amounts of products for their quantification. It is worth noting that even if the reconditioning step can be considered as a “dead

time" in the whole process, it accounts only for the 10% of the total electrolysis time (30 s every 270 s). The recovery of the initial current density values for the Foam-Au and Col-Au samples, moreover, suggested a good mechanical stability during the electrochemical measurements, which was attributed to the Cr adhesion layer between Au and the FTO substrate.

The Faradic efficiencies (FE) of the different products as a function of the applied bias are reported in Figure 6 and in Table S2. Col-Au electrodes yielded CO as the major CO_2 reduction product (up to 35% FE at the low $|\eta|$ value of 0.31 V), as well as small amounts (< 8%) of formic acid at –0.62 V (Figure 6a). At the same time, hydrogen also evolved, as a consequence of the competing proton reduction. Anyway, the H_2/CO ratio ~ 2 registered at intermediate bias (–0.42 and –0.52 V) is a particularly appealing gas mixture, being compatible with important industrial processes, such as hydrocarbons or methanol production via Fischer-Tropsch syntheses.[13,14,15]

On the other hand, the Foam-Au surface more markedly favors proton over CO_2 reduction (Figure 6b). Indeed, the maximum FE value for CO evolution was 13% at –0.42 V ($|\eta|$ = 0.31 V), still overcoming the Au foil, for which < 6% of carbon monoxide was observed in the whole investigated potential range (Figure 6c). The H_2/CO ratio for Foam-Au is thus > 2 (see Table S2 for further details), envisaging the use of these gaseous mixtures for the production of short-chain hydrocarbons (e.g. methane) via Fischer-Tropsch syntheses, being H_2 involved in chain termination processes.[15] Furthermore, the syngas mixtures with higher hydrogen content could be used for biological fermentations, since the specificity of the involved enzymatic reactions makes this kind of processes less dependent on fixed H_2/CO compositions. Indeed, syngas mixtures obtained from the pyrolysis of solid waste and organic residues were recently fed to microorganisms, yielding biodegradable plastics, such as polyhydroxyalkanoates (polyesters).[70,71]

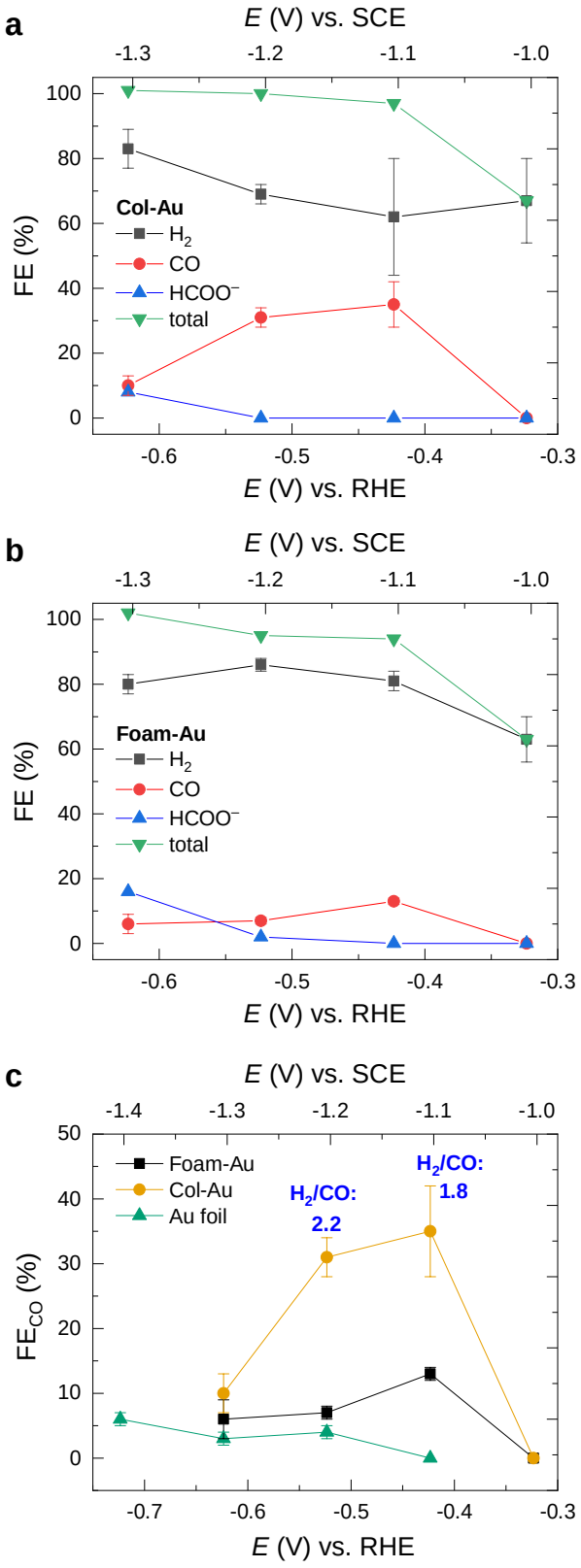

Figure 6. Faradic efficiency of the different products obtained with Col-Au (a) and Foam-Au (b) cathodes as a function of the applied bias. Each point is an average of at least 3 measurements, and the corresponding standard deviations are reported as error bars. The < 100% total FE observed at -0.32 V (low current, i.e. lower amount of products) can be due to a trapping of the gas products in stagnant corners of the

electrochemical cell. (c) Applied bias dependence of the faradic efficiency for the generation of CO for the different cathodes.

When compared to other nanoporous structures reported in the literature, which usually show the selective formation of CO in aqueous media (FE > 95%),[18,20,24, 25,32] both our cathodes produced significantly higher amounts of H_2, speaking in favor of a preferential absorption of *H over *CO_2 (likely as *COO^-) [52] on CoI-Au and Foam-Au surfaces. A possible explanation of this behavior could be related to a low amount of grain boundaries in our morphologies, mostly present in the foam-like domains of the Foam-Au film (Figure 3d) rather than in the vertically-oriented CoI-Au (Figure 1a) and in the bottom layer of the Foam-Au (Figure 1c). Indeed, the surface density of grain boundaries has been linearly correlated to CO_2 reduction activity.[26] On the other hand, the higher Faradic efficiency in CO production of the CoI-Au film with respect to the Foam-Au film (Figures 6a-b) could be related to a different relative abundance of under-coordinated facets, such as the (110), with respect to facets with high coordination number, such as (111) and (200). Indeed, XRD results (Figure 2) and TEM analysis (Figure 3) suggest a higher amount of (200) facets for the Foam-Au film. According to recent reports,[29] the equivalent (100) facets exhibit a significantly lower Faradic efficiency towards CO evolution rather than the under-coordinated (211) and (110). Consistently, the CoI-Au film, which exhibits a stronger (220) diffraction peak, i.e. equivalent to the (110) lattice planes family, produced a higher amount of CO. Moreover, the Au foil, mostly exhibiting the highly-coordinated (200) facets, produced very low amounts of CO (Figure 6c).

This aspect indirectly translates also in the different amount of irreversibly bridge-bonded CO spectators (CO_{bridge}) on the surface of the investigated cathodes. Indeed, using the oxidative stripping method described by the Surendranath group,[52] we could estimate the surface coverage of the CO_{bridge} spectators (see Figure S6, Experimental Section and Supporting Information for further details). Table S3 collects the calculated values, increasing in the order Au foil < Foam-Au < CoI-Au, thus confirming the preferential coordination of CO on under-coordinated sites.

On the other hand, the FE for CO of the Au foil was ≤ 6% (Figure 6c), similarly to previous studies [21,33] but lower than in others, reporting FEs ranging from 10% to 40%,[23,25,72] but also up to more than 90%.[29] The scattered FE_{CO} values reported in the literature may be in part due to molecular species adsorbed to the Au surface, which have shown the capability to regulate the selectivity of functionalized Au surfaces.[73] To elucidate this aspect, XPS measurements were performed on the CoI-Au and Foam-Au films (both before and after CO_2 reduction experiments), as well as on the Au foil (Figure S7 and Table S4), evidencing only Au, C and O peaks, thus ruling out any heterometallic

contamination within the detection limits of XPS. Furthermore, in all the samples the local chemical environment of the metallic Au surface was not affected by the electrochemical experiments (Figure S7). Substantial amounts of C and O in form of oxyhydrocarbons [74] were always detected, respectively ~40 and ~10 at. % for the nanostructured Au films, both for the pristine and tested samples, and ~56 and ~21 at. % for the Au foil (Table S4). Such high content of carbon detected on the Au foil surface [69] may be responsible for its unusually low FE towards CO.[73]

Finally, it is worth noting that the performance of the Au electrodes could also be affected by parameters related to the experimental set-up. In our case, the nanostructured Au cathodes likely experienced a progressive local depletion of the gaseous substrate over time due to the limited mass transport of CO_2, thus favoring H_2 formation. This limitation may mask the beneficial effects arising from the build-up of local pH gradients, reported to inhibit H_2 generation, thus enhancing the global CO_2-to-fuel selectivity.[52] In order to improve this aspect, we are currently optimizing a new custom-made electrochemical cell featuring a flow circulation of the electrolytic solution saturated with CO_2.

4. Conclusions

We have successfully prepared two nanostructured porous Au-cathodes through a one-step synthesis using pulsed laser deposition. By carefully tuning the deposition parameters, we could obtain high porosity morphologies, displaying either a quite regular columnar arrangement or a foamy structure. When used as cathodes for the electrochemical reduction of CO_2, the two electrodes displayed a selective production of syngas mixtures of different compositions already at overpotentials as low as 0.31 V in aqueous media. In particular, with the Col-Au cathodes we obtained a quantitative conversion of charge into syngas (faradic efficiency) with H_2/CO ratio ~ 2, the most appropriate composition for Fischer-Tropsch processes aimed at the production of hydrocarbons or methanol. On the other hand, the Foam-Au cathodes produced syngas mixtures enriched in H_2, which could be exploited either for the methane production or for biological fermentation to yield biodegradable plastics.

Starting from our results, one can envisage the design of reactors for the Fischer-Tropsch process or bioreactors directly fed by the gaseous mixture generated by our electrochemical cell, thus valorizing the waste gas CO_2 while changing the paradigm of the concomitant production of H_2 from a negative aspect to an asset.

Acknowledgements

The project leading to this application has received funding from the European Union's Horizon 2020 research and innovation programme under the Marie Skłodowska-Curie Grant Agreement No 705723. L. M. and A. Naldoni gratefully acknowledge support from the Operational Programme Research, Development and Education - European Regional Development Fund, project no. CZ.02.1.01/0.0/0.0/15_003/0000416 of the Ministry of Education, Youth and Sports of the Czech Republic. L. M. and A. Naldoni also thank Josef Kašlík, Jana Stráská, Ondřej Tomanec and Martin Petr (Regional Centre of Advanced Technologies and Materials, Faculty of Science, Palacký University Olomouc) for their aid in XRD, TEM, HRTEM and XPS measurements, respectively. B.R.B and A.L.B. acknowledge the Center for Nanophase Materials Sciences (CNMS) at Oak Ridge National Laboratory (ORNL) for the X-ray diffraction measurements under the User Project CNMS2018-309. M. G. acknowledges the financial support of the Polimi International Fellowship (PIF) programme. Mr. Stefano Doro and Mr. Claudio Niorettini from Laboratorio Audio S.N.C. are also gratefully acknowledged.

Supporting Information for Publication file

TEM and STEM-HAADF images; EDS mapping; DLC measurements for ECSA determination; Pictures of the set-up; Chronoamperometries and CO stripping analyses; XPS analysis.

TOC

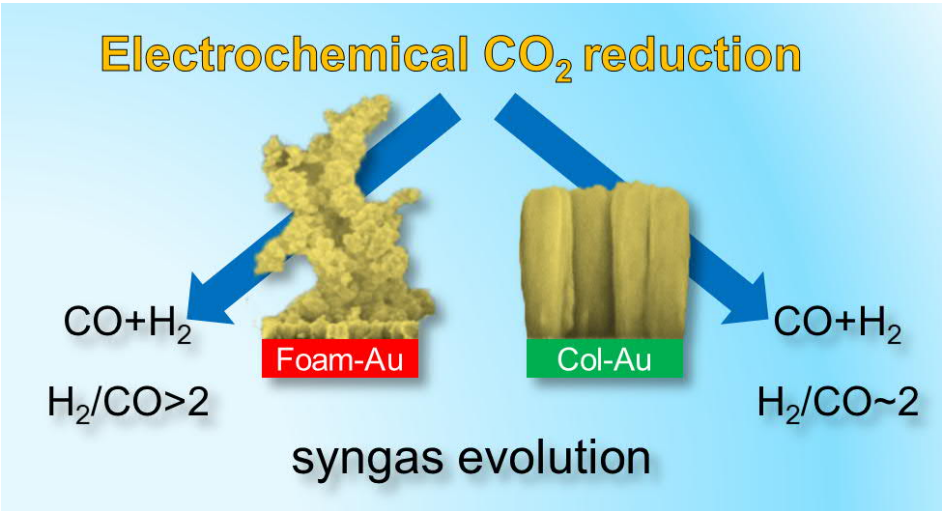

Bibliography

1. Griscom, B. W.; Adams, J.; Ellis, P. W.; Houghton, R. A.; Lomax, G.; Miteva, D. A.; Schlesinger, W. H.; Shoch, D.; Siikamäki, J. V.; Smith, P., Natural climate solutions. Proc. Natl. Acad. Sci. 2017, 114 (44), 11645-11650.
2. Fuss, S.; Lamb, W. F.; Callaghan, M. W.; Hilaire, J.; Creutzig, F.; Amann, T.; Beringer, T.; de Oliveira Garcia, W.; Hartmann, J.; Khanna, T., Negative emissions—Part 2: Costs, potentials and side effects. Environ. Res. Lett. 2018, 13 (6), 063002.
3. Vayenas, C. G.; White, R. E.; Gamboa-Aldeco, M. E., Modern Aspects of Electrochemistry 42. Springer Science & Business Media: 2008; Vol. 42.
4. Kuhl, K. P.; Hatsukade, T.; Cave, E. R.; Abram, D. N.; Kibsgaard, J.; Jaramillo, T. F., Electrocatalytic conversion of carbon dioxide to methane and methanol on transition metal surfaces. J. Am. Chem. Soc. 2014, 136 (40), 14107-14113.
5. Seh, Z. W.; Kibsgaard, J.; Dickens, C. F.; Chorkendorff, I.; Nørskov, J. K.; Jaramillo, T. F., Combining theory and experiment in electrocatalysis: Insights into materials design. Science 2017, 355 (6321), eaad4998.
6. Melchionna, M.; Bracamonte, M.; Giuliani, A.; Nasi, L.; Montini, T.; Tavagnacco, C.; Bonchio, M.; Fornasiero, P.; Prato, M., Pd@ TiO_2/carbon nanohorn electrocatalysts: reversible CO_2 hydrogenation to formic acid. Energy Environ. Sci. 2018, 11 (6), 1571-1580.
7. Dalle, K. E.; Warnan, J.; Leung, J. J.; Reuillard, B.; Karmel, I. S.; Reisner, E., Electro-and solar-driven fuel synthesis with first row transition metal complexes. Chem. Rev. 2019, 119 (4), 2752-2875.
8. Bagger, A.; Ju, W.; Varela, A. S.; Strasser, P.; Rossmeisl, J., Electrochemical CO_2 reduction: a classification problem. ChemPhysChem 2017, 18 (22), 3266-3273.
9. Huang, J.; Buonsanti, R., Colloidal nanocrystals as heterogeneous catalysts for electrochemical CO_2 conversion. Chem. Mater. 2018, 31 (1), 13-25.
10. Azuma, M.; Hashimoto, K.; Hiramoto, M.; Watanabe, M.; Sakata, T., Electrochemical reduction of carbon dioxide on various metal electrodes in low-temperature aqueous $KHCO_3$ media. J. Electrochem. Soc. 1990, 137 (6), 1772-1778.
11. Kuhl, K. P.; Cave, E. R.; Abram, D. N.; Jaramillo, T. F., New insights into the electrochemical reduction of carbon dioxide on metallic copper surfaces. Energy Environ. Sci. 2012, 5 (5), 7050-7059.
12. Zhang, Y.-J.; Sethuraman, V.; Michalsky, R.; Peterson, A. A., Competition between CO_2 reduction and H2 evolution on transition-metal electrocatalysts. ACS Catal. 2014, 4 (10), 3742-3748.
13. Dry, M. E., Practical and theoretical aspects of the catalytic Fischer-Tropsch process. Appl. Catal. A: Gen. 1996, 138 (2), 319-344.
14. Dry, M. E., The fischer–tropsch process: 1950–2000. Catal. Today 2002, 71 (3-4), 227-241.
15. Dry, M. E., High quality diesel via the Fischer–Tropsch process–a review. J. Chem. Technol. Biotechnol. 2002, 77 (1), 43-50.
16. Hori, Y.; Wakebe, H.; Tsukamoto, T.; Koga, O., Electrocatalytic process of CO selectivity in electrochemical reduction of CO_2 at metal electrodes in aqueous media. Electrochim. Acta 1994, 39 (11-12), 1833-1839.
17. Kortlever, R.; Shen, J.; Schouten, K. J. P.; Calle-Vallejo, F.; Koper, M. T., Catalysts and reaction pathways for the electrochemical reduction of carbon dioxide. J. Phys. Chem. Lett. 2015, 6 (20), 4073-4082.
18. Cave, E. R.; Montoya, J. H.; Kuhl, K. P.; Abram, D. N.; Hatsukade, T.; Shi, C.; Hahn, C.; Nørskov, J. K.; Jaramillo, T. F., Electrochemical CO_2 reduction on Au surfaces: mechanistic aspects regarding the formation of major and minor products. Phys. Chem. Chem. Phys. 2017, 19 (24), 15856-15863.
19. Narayanaru, S.; Chinnaiah, J.; Phani, K. L.; Scholz, F., pH dependent CO adsorption and roughness-induced selectivity of CO_2 electroreduction on gold surfaces. Electrochim. Acta 2018, 264, 269-274.
20. Chen, Y.; Li, C. W.; Kanan, M. W., Aqueous CO_2 reduction at very low overpotential on oxide-derived Au nanoparticles. J. Am. Chem. Soc. 2012, 134 (49), 19969-19972.
21. Lee, H.-E.; Yang, K. D.; Yoon, S. M.; Ahn, H.-Y.; Lee, Y. Y.; Chang, H.; Jeong, D. H.; Lee, Y.-S.; Kim, M. Y.; Nam, K. T., Concave rhombic dodecahedral Au nanocatalyst with multiple high-index facets for CO_2 reduction. ACS nano 2015, 9 (8), 8384-8393.

22. Zhu, W.; Zhang, Y.-J.; Zhang, H.; Lv, H.; Li, Q.; Michalsky, R.; Peterson, A. A.; Sun, S., Active and selective conversion of CO_2 to CO on ultrathin Au nanowires. J. Am. Chem. Soc. 2014, 136 (46), 16132-16135.
23. Kim, H.; Park, H. S.; Hwang, Y. J.; Min, B. K., Surface-morphology-dependent electrolyte effects on gold-catalyzed electrochemical CO2 reduction. J. Phys. Chem. C 2017, 121 (41), 22637-22643.
24. Liu, M.; Pang, Y.; Zhang, B.; De Luna, P.; Voznyy, O.; Xu, J.; Zheng, X.; Dinh, C. T.; Fan, F.; Cao, C., Enhanced electrocatalytic CO_2 reduction via field-induced reagent concentration. Nature 2016, 537 (7620), 382.
25. Welch, A. J.; DuChene, J. S.; Tagliabue, G.; Davoyan, A.; Cheng, W.-H.; Atwater, H. A., Nanoporous Gold as a Highly Selective and Active Carbon Dioxide Reduction Catalyst. ACS Appl. Energy Mater. 2019, 2 (1), 164-170.
26. Feng, X.; Jiang, K.; Fan, S.; Kanan, M. W., Grain-boundary-dependent CO_2 electroreduction activity. J. Am. Chem. Soc. 2015, 137 (14), 4606-4609.
27. Mariano, R. G.; McKelvey, K.; White, H. S.; Kanan, M. W., Selective increase in CO_2 electroreduction activity at grain-boundary surface terminations. Science 2017, 358 (6367), 1187-1192.
28. Zhang, W.; He, J.; Liu, S.; Niu, W.; Liu, P.; Zhao, Y.; Pang, F.; Xi, W.; Chen, M.; Zhang, W., Atomic origins of high electrochemical CO_2 reduction efficiency on nanoporous gold. Nanoscale 2018, 10 (18), 8372-8376.
29. Mezzavilla, S.; Horch, S.; Stephens, I. E.; Seger, B.; Chorkendorff, I., Structure sensitivity in the electrocatalytic reduction of CO_2 with gold catalysts. Angew. Chem. 2019, 131 (12), 3814-3818.
30. Todoroki, N.; Tei, H.; Tsurumaki, H.; Miyakawa, T.; Inoue, T.; Wadayama, T., Surface atomic arrangement dependence of electrochemical CO_2 reduction on Gold: online electrochemical mass spectrometric study on low-index au (hkl) surfaces. ACS Catal. 2019, 9 (2), 1383-1388.
31. Koh, J. H.; Jeon, H. S.; Jee, M. S.; Nursanto, E. B.; Lee, H.; Hwang, Y. J.; Min, B. K., Oxygen plasma induced hierarchically structured gold electrocatalyst for selective reduction of carbon dioxide to carbon monoxide. J. Phys. Chem. C 2014, 119 (2), 883-889.
32. Hall, A. S.; Yoon, Y.; Wuttig, A.; Surendranath, Y., Mesostructure-induced selectivity in CO_2 reduction catalysis. J. Am. Chem. Soc. 2015, 137 (47), 14834-14837.
33. Nesbitt, N. T.; Ma, M.; Trześniewski, B. J.; Jaszewski, S.; Tafti, F.; Burns, M. J.; Smith, W. A.; Naughton, M. J., Au Dendrite Electrocatalysts for CO_2 Electrolysis. J. Phys. Chem. C 2018, 122 (18), 10006-10016.
34. Kim, J.; Song, J. T.; Ryoo, H.; Kim, J.-G.; Chung, S.-Y.; Oh, J., Morphology-controlled Au nanostructures for efficient and selective electrochemical CO_2 reduction. J. Mater. Chem. A 2018, 6 (12), 5119-5128.
35. Mistry, H.; Reske, R.; Zeng, Z.; Zhao, Z.-J.; Greeley, J.; Strasser, P.; Cuenya, B. R., Exceptional size-dependent activity enhancement in the electroreduction of CO_2 over Au nanoparticles. J. Am. Chem. Soc. 2014, 136 (47), 16473-16476.
36. Kauffman, D. R.; Alfonso, D.; Matranga, C.; Qian, H.; Jin, R., Experimental and computational investigation of Au25 clusters and CO_2: a unique interaction and enhanced electrocatalytic activity. J. Am. Chem. Soc. 2012, 134 (24), 10237-10243.
37. Yang, B.; Mahjouri-Samani, M.; Rouleau, C. M.; Geohegan, D. B.; Xiao, K., Low temperature synthesis of hierarchical TiO 2 nanostructures for high performance perovskite solar cells by pulsed laser deposition. Phys. Chem. Chem. Phys. 2016, 18 (39), 27067-27072.
38. Geohegan, D. B.; Puretzky, A. A.; Duscher, G.; Pennycook, S. J., Time-resolved imaging of gas phase nanoparticle synthesis by laser ablation. Appl. Phys. Lett. 1998, 72 (23), 2987-2989.
39. Ghidelli, M.; Mascaretti, L.; Bricchi, B. R.; Zapelli, A.; Russo, V.; Casari, C. S.; Bassi, A. L., Engineering plasmonic nanostructured surfaces by pulsed laser deposition. Appl. Surf. Sci. 2018, 434, 1064-1073.
40. Canulescu, S.; Döbeli, M.; Yao, X.; Lippert, T.; Amoruso, S.; Schou, J., Nonstoichiometric transfer during laser ablation of metal alloys. Phys.Rev. Mater. 2017, 1 (7), 073402.
41. Bricchi, B. R.; Ghidelli, M.; Mascaretti, L.; Zapelli, A.; Russo, V.; Casari, C. S.; Terraneo, G.; Alessandri, I.; Ducati, C.; Bassi, A. L., Integration of plasmonic Au nanoparticles in TiO_2 hierarchical structures in a single-step pulsed laser co-deposition. Mater. Design 2018, 156, 311-319.
42. Casari, C. S.; Giannuzzi, C. S.; Russo, V., Carbon-atom wires produced by nanosecond pulsed laser deposition in a background gas. Carbon 2016, 104, 190-195.
43. Ojeda-G-P, A.; Döbeli, M.; Lippert, T., Influence of plume properties on thin film composition in pulsed laser deposition. Adv. Mater. Interfaces 2018, 5 (18), 1701062.

44. Gondoni, P.; Ghidelli, M.; Di Fonzo, F.; Russo, V.; Bruno, P.; Martí-Rujas, J.; Bottani, C. E.; Bassi, A. L.; Casari, C. S., Structural and functional properties of Al: ZnO thin films grown by Pulsed Laser Deposition at room temperature. Thin Solid Films 2012, 520 (14), 4707-4711.
45. Liu, Z.; Masel, R. I.; Chen, Q.; Kutz, R.; Yang, H.; Lewinski, K.; Kaplun, M.; Luopa, S.; Lutz, D. R., Electrochemical generation of syngas from water and carbon dioxide at industrially important rates. Journal of CO_2 Utilization 2016, 15, 50-56.
46. Fu, Q.; Mabilat, C.; Zahid, M.; Brisse, A.; Gautier, L., Syngas production via high-temperature steam/CO_2 co-electrolysis: an economic assessment. Energy Environ. Sci. 2010, 3 (10), 1382-1397.
47. Nguyen, V. N.; Blum, L., Syngas and synfuels from H_2O and CO_2: current status. Chem. Ing. Tech. 2015, 87 (4), 354-375.
48. Hernández, S.; Farkhondehfal, M. A.; Sastre, F.; Makkee, M.; Saracco, G.; Russo, N., Syngas production from electrochemical reduction of CO_2: current status and prospective implementation. Green Chemistry 2017, 19 (10), 2326-2346.
49. Sánchez, O. G.; Birdja, Y. Y.; Bulut, M.; Vaes, J.; Breugelmans, T.; Pant, D., Recent advances in industrial CO_2 electroreduction. Current Opinion in Green and Sustainable Chemistry 2019.
50. Wilhelm, D.; Simbeck, D.; Karp, A.; Dickenson, R., Syngas production for gas-to-liquids applications: technologies, issues and outlook. Fuel Process. Technol. 2001, 71 (1-3), 139-148.
51. Irtem, E.; Andreu, T.; Parra, A.; Hernández-Alonso, M.; García-Rodríguez, S.; Riesco-García, J.; Penelas-Pérez, G.; Morante, J., Low-energy formate production from CO_2 electroreduction using electrodeposited tin on GDE. J. Mater. Chem. A 2016, 4 (35), 13582-13588.
52. Wuttig, A.; Yaguchi, M.; Motobayashi, K.; Osawa, M.; Surendranath, Y., Inhibited proton transfer enhances Au-catalyzed CO_2-to-fuels selectivity. Proc. Natl. Acad. Sci. 2016, 113 (32), E4585-E4593.
53. Agarwal, N. R.; Neri, F.; Trusso, S.; Lucotti, A.; Ossi, P. M., Au nanoparticle arrays produced by pulsed laser deposition for surface enhanced Raman spectroscopy. Appl. Surf. Sci. 2012, 258 (23), 9148-9152.
54. Maffini, A.; Pazzaglia, A.; Dellasega, D.; Russo, V.; Passoni, M., Growth dynamics of pulsed laser deposited nanofoams. Phys.Rev. Mater. 2019, 3 (8), 083404.
55. Marine, W.; Patrone, L.; Luk'yanchuk, B.; Sentis, M., Strategy of nanocluster and nanostructure synthesis by conventional pulsed laser ablation. Appl. Surf. Sci. 2000, 154, 345-352.
56. McCrory, C. C.; Jung, S.; Ferrer, I. M.; Chatman, S. M.; Peters, J. C.; Jaramillo, T. F., Benchmarking hydrogen evolving reaction and oxygen evolving reaction electrocatalysts for solar water splitting devices. J. Am. Chem. Soc. 2015, 137 (13), 4347-4357.
57. Łukaszewski, M.; Soszko, M.; Czerwiński, A., Electrochemical methods of real surface area determination of noble metal electrodes–an overview. Int. J. Electrochem. Sci 2016, 11 (6), 4442-4469.
58. Trasatti, S.; Petrii, O., Real surface area measurements in electrochemistry. Pure Appl. Chem. 1991, 63 (5), 711-734.
59. McCrory, C. C.; Jung, S.; Peters, J. C.; Jaramillo, T. F., Benchmarking heterogeneous electrocatalysts for the oxygen evolution reaction. J. Am. Chem. Soc. 2013, 135 (45), 16977-16987.
60. Li, C. W.; Kanan, M. W., CO_2 reduction at low overpotential on Cu electrodes resulting from the reduction of thick Cu_2O films. J. Am. Chem. Soc. 2012, 134 (17), 7231-7234.
61. Mistry, H.; Varela, A. S.; Bonifacio, C. S.; Zegkinoglou, I.; Sinev, I.; Choi, Y.-W.; Kisslinger, K.; Stach, E. A.; Yang, J. C.; Strasser, P., Highly selective plasma-activated copper catalysts for carbon dioxide reduction to ethylene. Nature communications 2016, 7, 12123.
62. Yoon, Y.; Yan, B.; Surendranath, Y., Suppressing ion transfer enables versatile measurements of electrochemical surface area for intrinsic activity comparisons. J. Am. Chem. Soc. 2018, 140 (7), 2397-2400.
63. Hamelin, A.; Lipkowski, J., Underpotential deposition of lead on gold single crystal faces: Part II. General discussion. J. Electroanal. Chem. Interf. Electrochem. 1984, 171 (1-2), 317-330.
64. Hernández, J.; Solla-Gullón, J.; Herrero, E., Gold nanoparticles synthesized in a water-in-oil microemulsion: electrochemical characterization and effect of the surface structure on the oxygen reduction reaction. J. Electroanal. Chem. 2004, 574 (1), 185-196.
65. Singh, M. R.; Kwon, Y.; Lum, Y.; Ager III, J. W.; Bell, A. T., Hydrolysis of electrolyte cations enhances the electrochemical reduction of CO_2 over Ag and Cu. J. Am. Chem. Soc. 2016, 138 (39), 13006-13012.

66. Resasco, J.; Chen, L. D.; Clark, E.; Tsai, C.; Hahn, C.; Jaramillo, T. F.; Chan, K.; Bell, A. T., Promoter effects of alkali metal cations on the electrochemical reduction of carbon dioxide. J. Am. Chem. Soc. 2017, 139 (32), 11277-11287.
67. Thorson, M. R.; Siil, K. I.; Kenis, P. J., Effect of Cations on the Electrochemical Conversion of CO_2 to CO. J. Electrochem. Soc. 2013, 160 (1), F69-F74.
68. Wu, J.; Risalvato, F. G.; Ke, F.-S.; Pellechia, P.; Zhou, X.-D., Electrochemical reduction of carbon dioxide I. Effects of the electrolyte on the selectivity and activity with Sn electrode. J. Electrochem. Soc. 2012, 159 (7), F353-F359.
69. Kim, H.; Jeon, H. S.; Jee, M. S.; Nursanto, E. B.; Singh, J. P.; Chae, K.; Hwang, Y. J.; Min, B. K., Contributors to enhanced CO_2 electroreduction activity and stability in a nanostructured Au electrocatalyst. ChemSusChem 2016, 9 (16), 2097-2102.
70. Beneroso, D.; Bermúdez, J.; Arenillas, A.; Menéndez, J., Comparing the composition of the synthesis-gas obtained from the pyrolysis of different organic residues for a potential use in the synthesis of bioplastics. J. Anal. Appl. Pyrolysis 2015, 111, 55-63.
71. Brown, R. C., Hybrid thermochemical/biological processing. Appl. Biochem. Biotechnol. 2007, 137 (1-12), 947-956.
72. Kwok, K. S.; Wang, Y.; Cao, M. C.; Shen, H.; He, Z.; Poirier, G.; McCandless, B. E.; Livi, K. J.; Muller, D. A.; Wang, C., Nano-folded gold catalysts for electroreduction of carbon dioxide. Nano Lett. 2019, 19 (12), 9154-9159.
73. Fang, Y.; Flake, J. C., Electrochemical reduction of CO_2 at functionalized Au electrodes. J. Am. Chem. Soc. 2017, 139 (9), 3399-3405.
74. Miller, D.; Biesinger, M.; McIntyre, N., Interactions of CO_2 and CO at fractional atmosphere pressures with iron and iron oxide surfaces: one possible mechanism for surface contamination? Surface and Interface Analysis: An International Journal devoted to the development and application of techniques for the analysis of surfaces, interfaces and thin films 2002, 33 (4), 299-305.